Self-supported carbon nanofibers as negative electrodes for K-ion batteries: Performance and mechanism

Justine Touja, Vincent Gabaudan, Filippo Farina, Sara Cavaliere, Laure Caracciolo, Lénaïc Madec, Hervé Martinez, Athmane Boulaoued, Joachim Wallenstein, Patrik Johansson, et al.

Self-supported carbon nanofibers as negative electrodes for K-ion batteries: performance and mechanism

Justine Touja [ab], Vincent Gabaudan [ab], Filippo Farina [a], Sara Cavaliere [ac], Laure Caracciolo[bd], Lénaïc Madec[bd*], Hervé Martinez[bd], Athmane Boulaoued[e], Joachim Wallenstein[e], Patrik Johansson[ef], Lorenzo Stievano [abf], Laure Monconduit [abf*]

[a]*ICGM, Université de Montpellier, CNRS, Montpellier (France)*

[b]*Réseau sur le Stockage Électrochimique de l'Énergie (RS2E), CNRS, Amiens (France)*

[c]*Institut Universitaire de France (IUF), Paris, France.*

[d]*CNRS/ UNIV Pau & Pays Adour/ E2S UPPA, IPREM, UMR5254, 64000, Pau, France*

[e]*Department of Physics, Chalmers University of Technology, SE-412 96 Gothenburg, (Sweden)*

[f]*ALISTORE-European Research Institute, CNRS FR 3104, 80039 Amiens*

Abstract

Self-standing carbon nanofibers (CNF) were electrospun and tested in K-ion batteries (KIB). The comparison of the electrochemical performance of KIB using potassium bis(fluorosulfonyl)imide (KFSI) and potassium hexafluorophosphate (KPF_6) carbonate-based electrolytes revealed that, despite the coulombic efficiency is more readily stabilized with KFSI than with KPF_6, the long-term cycling is quite the same, with a specific capacity of 200 $mAh.g^{-1}$ for the CNF electrode. *Post-mortem* X-ray photoelectron spectroscopy analysis shows a more stable solid electrolyte interphase (SEI) for KIB employing KFSI. Finally, the K^+ ion storage mechanism was investigated by combining cyclic voltammetry and *operando* Raman spectroscopy, highlighting a combination of adsorption and intercalation processes. However the rate capability is better with the KPF_6 salt due to SEI layers formed at both CNF and K metal electrode, highlighting that full cell may lead to even superior results.

Corresponding author

Dr. Laure Monconduit: laure.monconduit@umontpellier.fr

Dr. Lénaïc Madec: lenaic.madec@univ-pau.fr

Keywords: K-ion batteries, Self-supported electrode, Carbon nanofibers, K^+ storage mechanism, Solid Electrolyte Interphase

Introduction

Lithium-ion batteries (LIB) have been widely employed for portable devices and electrical vehicles, but the limited resources and the uneven distribution of lithium cause great concerns for large scale application such as stationary energy storage. In the last decade, the research based on batteries working with Earth's crust abundant elements such as sodium or potassium has been widely developed.[1] Beyond the interest of using abundant elements that can lead to lower prices of precursors and electrolyte salts, potassium-ion batteries (KIB) exhibit in particular other significant advantages. For instance, the low standard potential of the K^+/K couple (-2.95 V *vs.* SHE) in organic EC:DEC solvents, even compared to Li^+/Li (-2.80 V *vs.* SHE) is promising for the development of high energy density batteries. Moreover, the high ionic conductivity of potassium-based electrolytes, deriving from the weak Lewis acidity of K^+, is favorable for the development of high power density batteries.

Regarding negative electrodes, as for LIB, most studies focus on carbonaceous materials such as graphite, hard carbon, or carbon nanotubes.[2,3] The electrochemical intercalation of potassium into graphite was studied by different groups using both *ex situ* and *in situ* characterization techniques, which showed a staging mechanism up to the formation of KC_8 with a theoretical capacity of 279 $mAh.g^{-1}$.[4–8] Very recently, outstanding performance (constant reversible capacity of around 255 $mAh.g^{-1}$ for over 2000 cycles) was obtained for KIB with graphite in high loading.[9] However, all such electrodes need to be formulated with a binder and supported on a current collector, which led to a dead volume/weight inside the battery and higher costs. Self-supported electrodes are thus of considerable interest in order to increase the overall energy density by removing the weight of binder, conductive additive, and current collector.[10] Self-standing electrodes made of carbon nanofibers (CNF) of different natures were tested in LIB, presenting good capacities ranging between 250 and 350 $mAh.g^{-1}$ at 30 $mA.g^{-1}$, which is close to the specific capacity of graphite (370 $mAh.g^{-1}$).[11–14] Similar performance (250 $mAh.g^{-1}$ at 50 $mAh.g^{-1}$) can be obtained for sodium-ion batteries.[15–18] More recently, CNF were applied as anodes for KIB (Table S1) delivering capacities near that of graphite.[19] The potassium storage mechanism for CNF has both capacitive and faradaic contributions whose proportions can be altered by the carbonization temperature. Higher temperatures lead to the formation of graphitic domains for potassium intercalation.[20] In contrast, oxygen functionalization increases the capacitive behavior.[21] Other modifications such as doping with heteroatoms,[22] or encapsulating CNTs in the fibers,[23] have been proposed to enhance the electronic conductivity and increase the active sites for potassium

storage. In most cases using CNF-based anodes, however, the first cycle coulombic efficiency (CE) is lower than 50 %, due to the electrolyte decomposition and the concomitant formation of a solid electrolyte interphase (SEI) at the electrode surface. Recently, it was shown that the use of potassium bis(fluorosulfonyl)imide (KFSI) as the electrolyte salt produces a much more efficient SEI than that formed in the more conventional potassium hexafluorophosphate (KPF_6) salt.[9,24,25]

In this work, we carefully investigate the electrochemical performance of self-supported CNF prepared by electrospinning as negative electrodes in KIB. As the performance is strongly influenced by the electrolyte, two different carbonate-based electrolytes were tested, using either KFSI or KPF_6 salts. To rationalize their performance in more detail, X-ray photoelectron spectroscopy (XPS) was performed to determine the nature and the evolution of the SEI upon cycling. Finally, a specific focus was put on understanding the electrochemical storage mechanism of the CNF by using a combination of cyclic voltammetry and *operando* Raman spectroscopy.

Results and discussion

Characterizations of CNF

The morphology of the CNF mat was examined using scanning electron microscopy (SEM) showing a uniform network with an average fiber diameter of 250 nm (Fig. 1a inset). The X-ray diffraction (XRD) pattern (Fig. 1a) revealed a broad peak at $2\theta = 25°$ corresponding to the (002) reflection of graphite and a small large contribution centered at 43° corresponding to the (101) reflections of a turbostratic carbon structure.[26] The Raman spectrum (Fig 1b) displays two bands at 1350 and 1580 cm^{-1}, corresponding to the disordered (D-band) and graphitized (G-band) sp^2 carbon, respectively. The I_D/I_G ratio of 1.7 calculated by fitting the spectrum with three Lorentzian and two Gaussian components indicates a disordered structure with local graphite inclusions (turbostratic domains) typical of electrospun PAN-derived CNF (Fig. S1).[26–29] The presence of these turbostratic domains is confirmed with the transmission electron microscopy (TEM) image (Fig. 1c). The nitrogen adsorption-desorption curve of CNF, which is a type IV isotherm with type H3 hysteresis loop, corresponds to a meso/macro porous structure with a Brunauer-Emmet-Teller (BET) surface area of 30 $m^2.g^{-1}$ and an average pore width of 5 nm (Fig. 1d). The electronic conductivity of the self-standing mat was *ca.* 30 $S.cm^{-1}$.[30] The carbon 1s and oxygen 1s XPS

core spectra (Fig. 1e, 1f), from which a sp^2/sp^3 ratio of ~23 was calculated, indicate that the carbon is mostly graphitic, but that a consistent amount of non-graphitic carbon is also present. Altogether, the bulk (XRD), the close-to-surface (Raman), and the surface (XPS) assessments of the degree of graphitization show that the fibers contain ordered graphitized domains of relatively small sizes (< 2.5 nm, according to Raman spectroscopy).

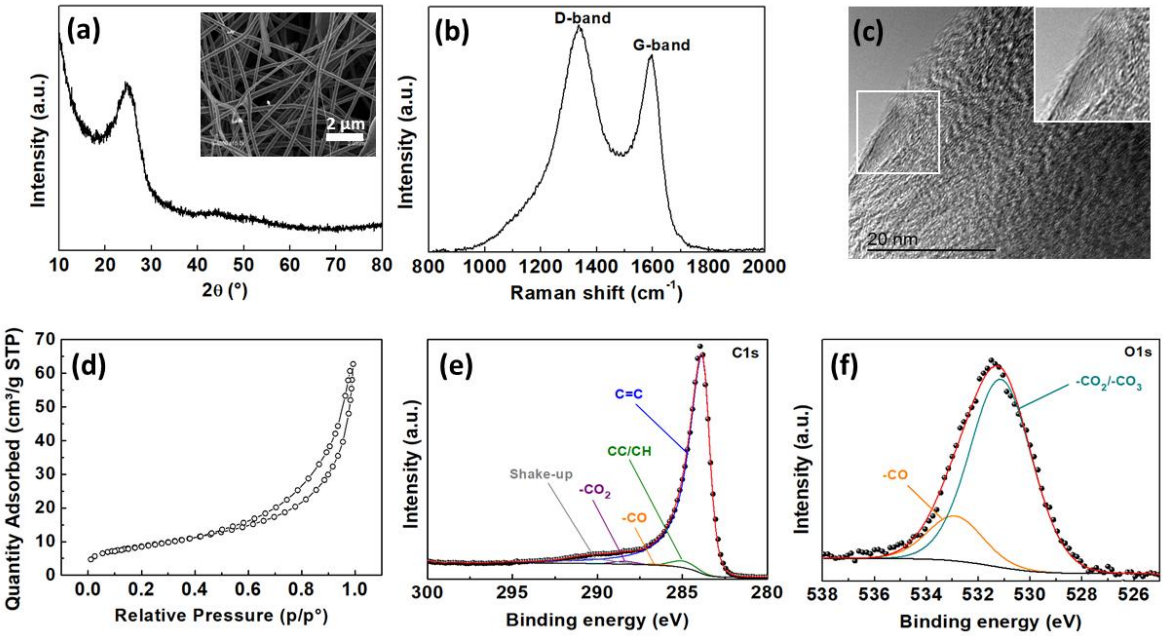

Figure 1. Characterization of the pristine self-supported mat of CNF. (a) XRD pattern with SEM image (inset), (b) Raman spectrum, (c) TEM image, (d) nitrogen adsorption/desorption isotherm, and XPS spectra (e) of C 1S and (f) O 1s regions.

Half-cell cycling performance

The electrochemical performance of the CNF mats as KIB negative electrodes was evaluated in half-cells vs. K metal using 0.8 M KFSI in EC:DEC and 0.8 M KPF_6 in EC:DEC electrolytes (Fig. 2). Overall, whatever the electrolyte, the galvanostatic profiles (Fig. 2a, d) exhibit three distinct pseudo-plateaus at 0.7, 0.5 and 0.2 V during the first discharge.

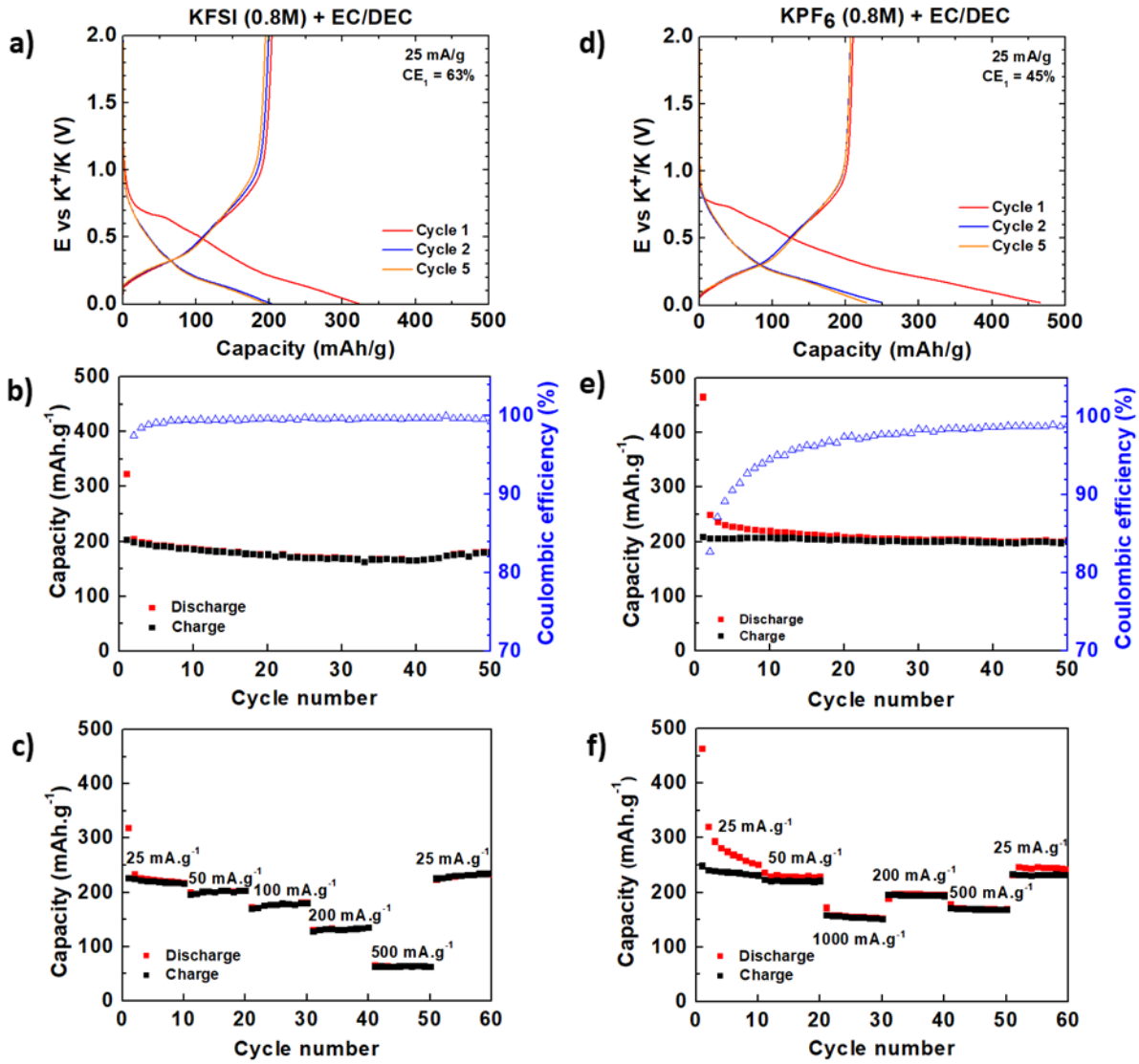

Figure 2. Electrochemical performance of CNF vs K. Galvanostatic charge/discharge at 25 mA.g^{-1}, capacity retention and C-rate with 0.8 M KFSI (a-c) and KPF_6 (d-f) in EC:DEC.

The first irreversible plateau at 0.7 V can be attributed to the formation of the SEI, occurring mainly during the first cycle. A significant difference in reversibility is observed as a function of the salt: the KFSI-based electrolyte shows a much better CE (63%) than the KPF_6-based one (45%). The latter performance is better than most data in the literature, all of which were cycled with a KPF_6-based electrolyte (Table S1).[19–21] Moreover, the stabilization of the CE takes longer to reach for the KPF_6-based electrolyte: 99.5% is reached first after 50 cycles, whereas only 10 cycles are needed for the KFSI-based electrolyte. A capacity retention of *ca.* 200 mAh.g^{-1} over 50 cycles is obtained for both electrolytes (Fig. 2b, e). Thus the SEI seems to be less efficient for the first cycles with KPF6, but after thirty cycles it stabilizes and the batteries performance are very close.

The rate capability test, using current densities from 25 $mA.g^{-1}$ to 1000 $mA.g^{-1}$, (Fig. 2c, f), shows both lower capacities at low rate and a more rapid capacity fading for the KFSI-based electrolyte (only 60 $mAh.g^{-1}$ at 500 $mA.g^{-1}$), while the KPF_6-based electrolyte can sustain a capacity of 150 $mAh.g^{-1}$ at 1000 $mA.g^{-1}$. The better performance of CNF with KPF6 electrolyte when the current is increased may be due to the fact that the electrolyte decomposition is reduced at high current rates. It is worth noticing that both salts show close ionic conductivities at room temperature, 7.9 and 10.6 $mS.cm^{-1}$ for KPF_6 (0.8M) and KFSI (0.8M) in EC:DEC respectively. On the other hand it is now well known that the high reactivity of K metal results in specific reaction of electrolytes on its surface, which can influence the other electrode/electrolyte interface via a cross-talk mechanism.[31] Thus we have simply measured the polarization of the K plating/stripping of K//Al cells as function of the rate (corresponding to the C-rate used in Figure 2) for 0.8 M KFSI and 0.8 M KPF_6 in EC:DEC. The latter shows a lower polarization (Fig. S2), thus highlighting that full (with CNF electrode) cell may lead to better rate capability.

In both electrolytes, the CNF electrodes withstand these high current densities without being damaged, since they retain capacities close to initial ones when back to a lower current density, *i.e.*, 130 $mAh.g^{-1}$ (KFSI) and 200 $mAh.g^{-1}$ (KPF_6) at 200 $mA.g^{-1}$, which is higher than graphite, known to suffer at high current densities.[8]

SEI passivation/ stability

As the high electrolyte reactivity at the K metal surface can produce electrolyte degradation species able to migrate to the CNF electrodes, the SEI at the CNF surface may arise from electrolyte degradation generated at both the K metal and CNF electrodes, as previously been demonstrated.[31] As a consequence, as function of electrolyte the electrode/electrolyte interface can hereby be heavily modified and impact the battery performance. To rationalize the different electrochemical behavior observed, especially the coulombic efficiency (CE), XPS was measured to identify the SEI layer. After the first cycle, both the C 1s and the O 1s core spectra have completely changed compared to the pristine electrode, by coverage by electrolyte degradation species, resulting in a large decrease of the C=C peak from the CNF (Fig. S3, Tables S2, S3). From the XPS quantification data, the content of each species (in at.%) detected at the CNF electrodes surface after 1 cycle and 50 cycles was determined (Fig. 3, Table S2 and S3). For the KPF_6-based electrolyte, ~70 at.% consists of organic species (ROCOOK, PEO and other -CO containing species), the remainder

being inorganic species (K_2CO_3 and KOH). In contrast, the KFSI-based electrolyte produces a much lower content of organic species; ~35 at.% (mainly ROCOOK, and few PEO and other -CO containing species), while much more salt degradation products including KF, that was not observed for KPF_6, are formed (~65 at.%). After 50 cycles, the amount of ROCOOK increases for both KPF_6 (46 to 62 at.%) and KFSI (34 to 56 at.%) -based electrolytes, suggesting a relatively higher rate of accumulation of carbonate-based solvent degradation species.[9,24,25] At first sight, this might appear surprising in the light of the much lower CE for the KPF_6-based electrolyte (Fig. 2) and the recent literature reporting the formation of thinner SEI with KFSI. This can, however, be explained by the formation of a more stable SEI at the CNF surface with KFSI, so that new organic species can accumulate over cycling, whereas a less stable SEI is formed with KPF_6, so that organic species accumulation is hindered. This likely produces the higher ratio of inorganic/organic species after 50 cycles for the KFSI-based cell (0.6) as compared to the KPF_6-based cell (0.3).

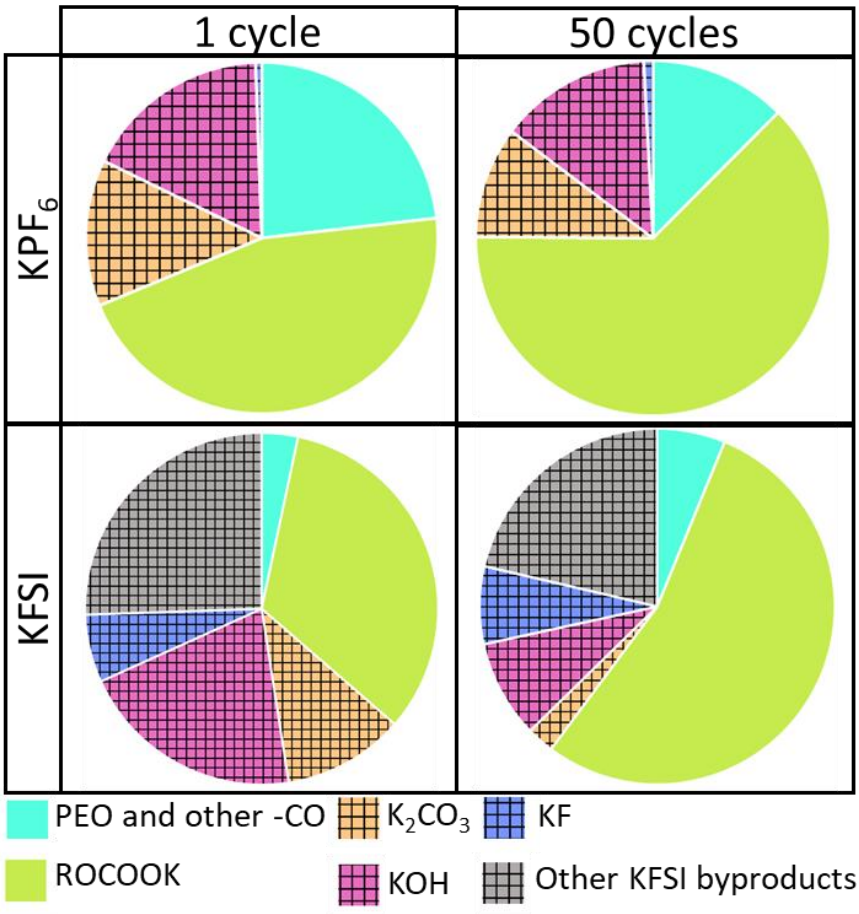

Figure 3. SEI composition as derived from XPS quantification of CNF electrodes recovered from CNF/K cells after 1 and 50 cycles), using 0.8 M of either KFSI or KPF_6 in EC:DEC as electrolyte. Striped/plain areas highlight inorganic/organic species.

K^+-ion storage mechanism

Cyclic voltammetry (CV) and *operando* Raman spectroscopy were used together to elucidate the extent and role of the different possible storage mechanisms when using CNF-based negative electrodes. With CV, the redox behavior of the potassiation/depotassiation mechanism is targeted. The results for the KFSI-based electrolyte are shown in Fig. 4, whereas those of the KPF_6-based one are shown in Fig. S4. In the first CV scan of two, three reduction peaks are observed at 0.8, 0.4 and 0.02 V and two oxidation peaks at 0.45 and 0.8 V (Fig. 4a), all in agreement with the galvanostatic profile.

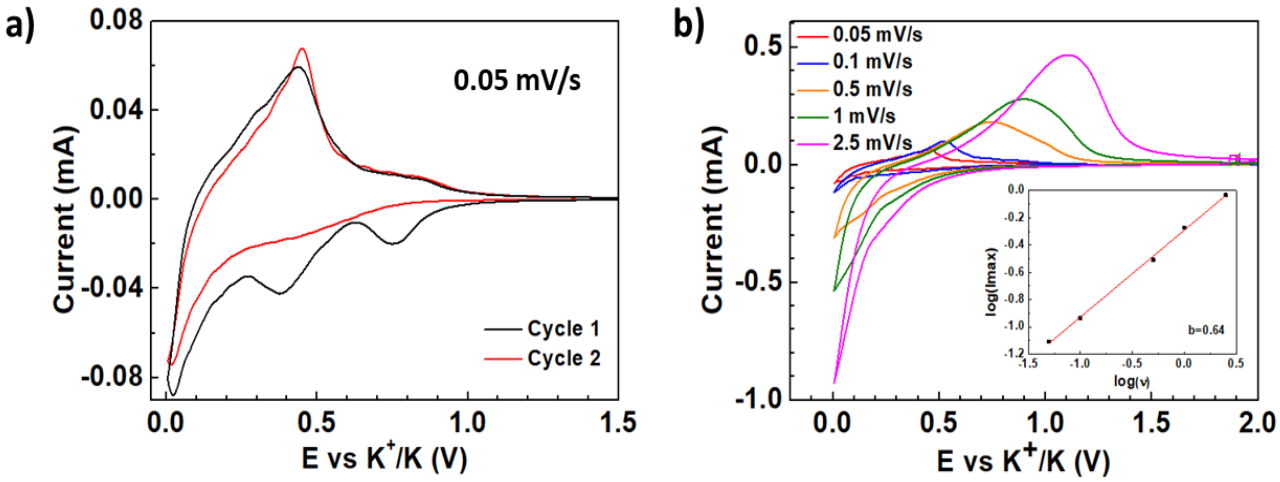

Figure 4. Cyclic voltammetry of CNF using 0.8 M KFSI in EC:DEC at 0.05 mV/s (a) and cyclic voltammetry at different scan rates from 0.05 to 2.5 mV/s (b).

Using different CV scan rates results in a cathodic peak at 0.02 V and an anodic peak shifting from 0.4 V to 1.1 V as a function of scan rate (Fig. 4b). This can be analyzed using the following equation:[32]

$$i = av^b,$$

where i is the peak current, v the scan rate, and a and b are constants that can be derived by performing CV at different scan rates. b indicates whether the K^+ storage mechanism is faradaic, $b = 0.5$, or capacitive, $b = 1$. Here, b values of 0.64 and 0.86 are obtained for the

KFSI- and the KPF_6-based electrolyte, respectively, suggesting both faradaic and capacitive contributions in both cases, even though with a stronger faradic contribution for the KFSI-based electrolyte. Similar measurements done by Lin *et al.* for CNF derived from PAN carbonized at 1250 °C using a KPF_6-based electrolyte gave $b = 0.66$.[20]

These results are rather surprising, since the choice of salt anion in principle is not supposed to influence the potassiation mechanism of CNF. Nevertheless, these results confirm the different rate capability tests for the two systems, since a better performance is observed when using a KPF_6-based electrolyte, which also shows the strongest pseudocapacitive contribution. Indeed, the pseudocapacitive mechanism is expected to be faster and less resistive than the intercalation-induced faradaic reaction.[20]

The *operando* Raman spectroscopy study (Fig. 5) focusing on the two main CNF bands, D and G (typical of carbonaceous materials with sp^2 carbon hybridization) shows two large and partially overlapping bands, characteristic of disordered graphitic structures at OCP (*ca.* 2.9 V). The D band centered at ~1350 cm^{-1} is due to the ring breathing mode of A_{1g} symmetry, while the G band at ~1580 cm^{-1} is attributed to the in-plane bond-stretching with E_{2g} symmetry.[33–37] The capacity of the first discharge (~600 $mAh.g^{-1}$) in the *operando* set-up is noticeably higher than the ca. 300 $mAh.g^{-1}$ obtained in coin cells.

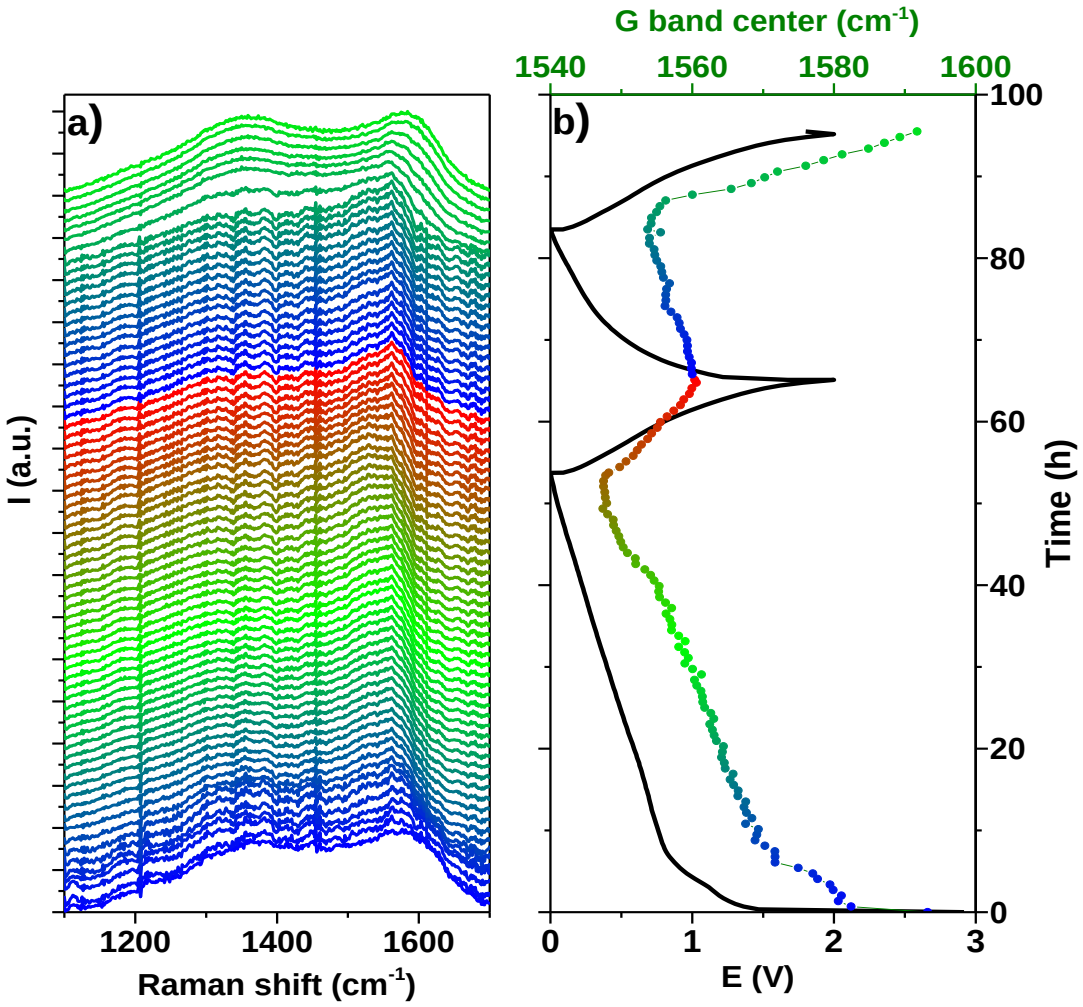

Figure 5. Operando Raman spectra (a) along with the corresponding electrochemical cycling charge-discharge curves and the G band position (b) for the CNF electrodes using the KFSI-based electrolyte.

This could be due to the large volume of electrolyte used in the *in situ* cell, inducing additional electrolyte degradation, and is in line with the lower capacity of ~300 mAh.g^{-1} obtained in the second discharge, where the parasitic reactions can arguably be inhibited by the electrode passivation. Upon discharge, the K^+ insertion induces a significant red shift of ~45 cm^{-1} of the G band (Fig. 5). This lowering is due to bond weakening in the distorted rings and concomitant softening of the vibrational density of states.[38] A deeper analysis of the band modification shows a relatively fast shift of the G band as function of discharge during the first slope region, until ~0.7 V, then the shift is slower during the second slope (0.7-0.25 V), with the shift roughly proportional to the voltage decrease rate. Finally, a steeper shift step follows, starting from ~0.25 V until the end of discharge.

Relying on already existing models for disordered carbons,[39,40] we ascribe these three stages to the following K^+-ion storage mechanisms: first adsorption on defects and edges of graphitic sheets, which are favorable sites for adsorption,[41,42] then intercalation within inter-planar space, and finally insertion in the pores. Some potassium plating is also possible at the very end of the discharge, corresponding to the small flat part in the G band position curve. For graphite intercalated with potassium, the G band splits into two components as stage VI proceeds,[43] and as this is not observed here, which might indicate some more random insertion of K^+ within the graphitic domains of the CNF electrode.[20]

For the D band, known to stem from defects and disorder in graphite nanocrystals,[34,44] the position remains virtually unchanged. However, its intensity decreases and its width increases upon K^+ insertion, which can be attributed to structural disorder induced by the adsorption of K^+ at sites where the graphitic structure is not fully developed, such as defects and edges. Moreover, just as an expanded graphite structure is well-known to help Na^+ intercalation,[45–47] we believe that the K^+ intercalation phase (the second long slope), is assisted by the prior adsorption on defect and edges of graphene (first slope), providing an expansion of the inter-layer spacing.

Conclusions

Self-standing mats of CNF were prepared by carbonization of electrospun polyacrylonitrile. They were directly used without any additional binder and conductive additive as negative electrodes *vs* K in KFSI and KPF_6 in EC:DEC electrolytes. In both cases, a stable capacity around 200 $mAh.g^{-1}$ was obtained over 100 cycles with promising rate capability, especially with KPF_6. Although similar capacity retention was obtained for both electrolytes, the coulombic efficiency takes longer time to stabilize near to 99 % with KPF_6 compared to KFSI. This distinct evolution prompted us to investigate the SEI composition and its growth during cycling for both electrolytes. The K^+ storage mechanism was deduced from CV and *operando* spectroscopy analysis as being a three stages process: adsorption on defect and edges of graphitic sheets, intercalation within the inter-plane space and insertion in the porosity. This storage mechanism is in good agreement with the conclusion of the CV analysis, which suggests a mixed faradic/capacitive mechanism.

The XPS analysis of the SEI demonstrates that the low CE observed for first cycles with KPF_6 is due to the formation of poorly efficient (*i.e.*, unstable and/or not passivating) SEI at the surface of both K metal and CNF electrodes. On the contrary, the use of 0.8 M KFSI in

EC:DEC triggers the formation of a more efficient (*i.e.*, more stable and passivating) SEI at the surface not only of the CNF electrode but also of the K metal leading to higher CE from first cycles. Overall, these results highlight the crucial role of the K metal reactivity/passivation in half cell studies compared to most of the literature that neglects the K metal impact on the electrochemical performance. A more precise determination of the reactivity of K metal against the commonly used KPF_6 and KFSI EC:DEC electrolytes is currently under investigation and will be the object of a forthcoming article, but preliminary results showed that a higher polarization is measured when KFSI EC:DEC is used, resulting in a lower rate capability. The better rate capability of the CNF electrode in KPF_6 based electrolyte is likely due to SEI layers formed at both CNF and K metal electrode.

The understanding of the complex SEI formation, its dependence upon the electrolyte composition and its evolution upon cycling is mandatory for the development of KIB. This work underlines the significant impact of the salt anion on the performance of negative electrode materials and open the way to the development of optimized electrolytes for KIB.

Experimental section

Synthesis

Self-standing CNF mats were prepared by carbonization of an electrospun polyacrylonitrile (PAN) mat with a process also described elsewhere.[30] Briefly, PAN precursor solutions were prepared dissolving the desired amount in N,N-dimethylformamide (DMF) and stirred overnight. The typical solution 8.5 % PAN/DMF was prepared dissolving 0.85 g of polymer (Sigma Aldrich, M_W = 150,000) in 9.15 g of solvent (Sigma Aldrich, 98% purity). The obtained solution was then electrospun for 8 h using a Spraybase® rotating drum system (100 rpm) with an applied potential of 15 kV, a flow rate of 1.0 $mL.h^{-1}$ and a needle tip-target distance of 10 cm. The resulting PAN nanofibrous mats were stabilized in oven in air: a first step at 150 °C allows to dehydrate the sample, while a second step at 270 °C allows the cyclisation of the polymer; the dwelling times were set at 2 and 3 hours respectively, while both heating ramps were set at 2.5 °C min^{-1}. The obtained mats were carbonized in a tubular oven under inert gas flow (argon) and heated at 4 °C.min^{-1} up to 1500 °C, leading to a self-standing mat of CNF. The carbonization temperature was held for 2 hours and then the oven cooled down naturally.

Characterization

Scanning electron microscopy (SEM) images were acquired with a Hitachi S-4800 electron microscope. XRD data were recorded with a PANalytical X'Pert Pro MPD diffractometer with a Cu Kα radiation source (λ=1.5418 Å) and a step size of 0.033° between 10° and 80°. *Ex situ* Raman spectrum was obtained with a Horiba Jobin-Yvon LabRAM ARAMIS spectrometer with an excitation wavelength of 473 nm. The CNF morphology was characterized with a JEOL 2200FS transmission electron microscope (TEM) operating at 200 kV, equipped with a CCD camera GATAN USC (17 million pixels). For the TEM analysis, the samples were suspended in ethanol and deposited after sonication (VWR Ultrasonic Cleaner) onto copper grids coated with carbon. Nitrogen adsorption/desorption isotherms were determined at -196 °C by means of a TriStar II, Micromeritics apparatus after outgassing overnight at 200 °C under vacuum (10^{-3} Pa). The specific surface area was calculated by using the Brunauer-Emmett-Teller (BET) equation and taking 0.162 nm^2 as the cross-sectional area of one N_2 molecule. The pore-size distribution was calculated from the adsorption branch of the adsorption-desorption isotherms by the Barrett-Joyner-Halenda equation. Electrical conductivity was measured using a 2400 Keithley in a 4-wire configuration on a 5 x 40 x 0.05 mm carbon electrode strip in a Fumatech MK3-L cell operated in the current range 0-100 mA.

Operando Raman spectroscopy

After the voltage value at OCP is stabilized (usually it takes few hours), a slow C/25 (assuming a theoretical capacity of 300 $mAh.g^{-1}$) discharge–charge galvanostatic cycling was performed using a GAMRY Series G300 potentiostat, in the range of 1.5 - 0 V versus K^+/K. The Raman spectra were collected at room temperature by a nitrogen-cooled CCD detector connected to a Dilor XY 800 spectrometer (Horiba GmbH), equipped with a 514 nm Ar/Kr laser operated with a power of 50 mW at the excitation source (< 2 mW on the sample surface), 1800 grooves/mm grating, 300 mm focal length and pinhole size of 400 µm. The spectra were collected in the backscattering geometry with 50X objective (confocal micro-Raman mode). Each spectrum was the average of 10 accumulations of 2 min each at a resolution of 2 cm^{-1}. The focal plane was adjusted to be at the electrode surface and very close to the edge of the aperture in the current collector, so that to lessen in-homogeneity of the electric field lines distribution on the probed spot. Before carrying out the *operando* experiments, we have checked first the stability of the electrode with the same Raman set-up described above. During more than 12 hours of continuous illumination of the electrode, the

I_D/I_G ratio, the peak positions and general shape of the spectra remained unchanged. Therefore, there is no significant effect of the laser on the graphitization degree and the structure of the CNF. Spectral processing consisted essentially of performing spikes removal, smoothing of noisy spectra, baseline correction, normalization and fitting. These steps were achieved using Origin-lab (V.8) and MATLAB (R2017b) software. To fit the D and G band of disordered carbons, many models have been used in literature. The most common one consists of five functions around 1100, 1350, 1500, 1580, 1620 cm^{-1}. This model however lacks physical significance.[37,48] Moreover, this model for the case of carbons where the G and D bands are exposed to deep modifications - like of the kind encountered in electrochemical cycling, it makes it hard to follow the changes of so many peaks. In this work, we have explored systematically several routines to deconvolve the spectra using models with different combinations of Lorentzian (L), Gaussian (G), as well as Breit–Wigner–Fano (BWF) profile bands (See r^2 values compared in Fig.S5, S6). The best fit (Fig. S5, S6) was achieved with a model consisting of 2 co-centered Lorentzians for D band, one Lorentzian for G band and one Gaussian situated between D and G accounting for sp^3 carbon of amorphous carbon.[35,36,49]

X-ray Photoelectron Spectroscopy

XPS was performed using an Escalab 250 Xi spectrometer using a monochromatized Al Kα radiation (hν=1486.6 eV). Electrode samples were put on a sample holder using an insulating uPVC tape (reference 655 from 3M). Then the samples transfer was performed through an argon-filled glovebox directly connected to the spectrometer, in order to avoid moisture/air exposure of the samples. Analysis was performed using the standard charge compensation mode and an elliptic 325 x 650 µm X-ray beam spot. Core spectra were recorded using a 20 eV constant pass energy with a 0.15 eV step size and iterative scans at a dwell time of 500 ms. Using CasaXPS software, the binding energy scale was calibrated from the 285.0 eV peak (C-C/C-H). A non-linear Shirley-type background was used for core peaks analysis while 70% Gaussian - 30% Lorentzian Voigt peak shapes and full width at half-maximum constraint ranges were selected to optimize areas and peak positions.

Electrochemical measurements

CNF discs with a diameter of 12 mm and a mass loading of 1 $mg.cm^{-2}$ were cut in the mat, dried overnight at 80°C under dynamic vacuum and used as self-supported electrodes in

CR2032 type coin cells (stainless steel 304L) assembled in an argon-filled glovebox. Potassium metal (Sigma Aldrich) was used as counter and reference electrodes and a glass fiber (Whatman, GF/D) as the separator soaked with 0.8 M KFSI (purity 99.9 %, Solvionic) or KPF_6 (purity 99%, Solvionic) dissolved in a 1:1 (v:v) mixture of ethylene carbonate (EC, anhydrous, purity 99 %, Alfa Aesar)/diethylene carbonate (DEC, anhydrous, purity 99 %, Sigma Aldrich). The electrochemical measurements were performed with a MTI battery tester between 0 and 2 V. Cyclic voltammetry curves were conducted on BCS cycler (Biologic).

Acknowledgements:

The authors thank the analysis and characterization platform from the "Pôle Chimie Balard". The research leading to these results has received funding from the European Research Council under the European Union's Seventh Framework Program (FP/2007–2013)/ERC Grant Agreement SPINAM no. 306682. SC acknowledges IUF for financial support. We warmly thank the Alistore-European Research Institute (ERI) network for the active collaboration between the two members, the Chalmers University and ICGM. The authors acknowledge also the French RS2E Network (RS2E) (STORE-EX Labex ProjectANR-10-LABX-76-01).

Declaration of interests

☒ The authors declare that they have no known competing financial interests or personal relationships that could have appeared to influence the work reported in this paper.

REFERENCES

[1] K. Kubota, M. Dahbi, T. Hosaka, S. Kumakura, S. Komaba, *Chem. Rec.* **2018**, *18*, 459–479.

[2] X. Wu, Y. Chen, Z. Xing, C. W. K. Lam, S. Pang, W. Zhang, Z. Ju, *Adv. Energy Mater.* **2019**, *9*, 1900343.

[3] V. Gabaudan, L. Monconduit, L. Stievano, R. Berthelot, *Front. Energy Res.* **2019**, *7*, 46.

[4] S. Komaba, T. Hasegawa, M. Dahbi, K. Kubota, *Electrochem. Commun.* **2015**, *60*, 172–175.

[5] J. Zhao, X. Zou, Y. Zhu, Y. Xu, C. Wang, *Adv. Funct. Mater.* **2016**, *26*, 8103–8110.

[6] J. C. Pramudita, V. K. Peterson, J. A. Kimpton, N. Sharma, *Powder Diffr.* **2017**, *32*, S43–S48.

[7] J. Liu, T. Yin, B. Tian, B. Zhang, C. Qian, Z. Wang, L. Zhang, P. Liang, Z. Chen, J. Yan, et al., *Adv. Energy Mater.* **2019**, *9*, 1900579.

[8] Z. Jian, W. Luo, X. Ji, *J. Am. Chem. Soc.* **2015**, *137*, 11566–11569.

[9] L. Fan, R. Ma, Q. Zhang, X. Jia, B. Lu, *Angew. Chemie Int. Ed.* **2019**, *58*, 10500–10505.

[10] Z. Yan, M. N. Obrovac, *J. Power Sources* **2020**, *464*, 228228.

[11] C. Kim, K. S. Yang, M. Kojima, K. Yoshida, Y. J. Kim, Y. A. Kim, M. Endo, *Adv. Funct. Mater.* **2006**, *16*, 2393–2397.

[12] M. H. Kjell, E. Jacques, D. Zenkert, M. arten Behm, G. Lindbergh, *J. Electrochem. Soc.* **2011**, *158*, A1455–A1460.

[13] J. Hagberg, S. Leijonmarck, G. Lindbergh, *J. Electrochem. Soc.* **2016**, *163*, A1790–A1797.

[14] G. Fredi, S. Jeschke, A. Boulaoued, J. Wallenstein, M. Rashidi, F. Liu, R. Harnden, D. Zenkert, J. Hagberg, G. Lindbergh, et al., *Multifunct. Mater.* **2018**, *1*, 015003.

[15] J. Jin, B. J. Yu, Z. Q. Shi, C. Y. Wang, C. Bin Chong, *J. Power Sources* **2014**, *272*, 800–807.

[16] S. Wang, L. Xia, L. Yu, L. Zhang, H. Wang, X. W. D. Lou, *Adv. Energy Mater.* **2016**, *6*, 1502217.

[17] Y. Liu, F. Fan, J. Wang, Y. Liu, H. Chen, K. L. Jungjohann, Y. Xu, Y. Zhu, D. Bigio, T. Zhu, et al., *Nano Lett.* **2014**, *14*, 3445–3452.

[18] W. Li, L. Zeng, Z. Yang, L. Gu, J. Wang, X. Liu, J. Cheng, Y. Yu, *Nanoscale* **2014**, *6*, 693–698.

[19] X. Zhao, P. Xiong, J. Meng, Y. Liang, J. Wang, Y. Xu, Y. Chen, X. Li, K. Park, J. Song, et al., *J. Mater. Chem. A* **2017**, *5*, 19237–19244.

[20] X. Lin, J. Huang, B. Zhang, *Carbon N. Y.* **2019**, *143*, 138–146.

[21] R. A. Adams, J.-M. Syu, Y. Zhao, C.-T. Lo, A. Varma, V. G. Pol, *ACS Appl. Mater. Interfaces* **2017**, *9*, 17872–17881.

[22] Y. Xu, C. Zhang, M. Zhou, Q. Fu, C. Zhao, M. Wu, Y. Lei, *Nat. Commun.* **2018**, *9*, 1720.

[23] C. Shen, K. Yuan, T. Tian, M. Bai, J. G. Wang, X. Li, K. Xie, Q. G. Fu, B. Wei, *ACS Appl. Mater. Interfaces* **2019**, *11*, 5015–5021.

[24] L. Deng, Y. Zhang, R. Wang, M. Feng, X. Niu, L. Tan, Y. Zhu, *ACS Appl. Mater. Interfaces* **2019**, *11*, 22449–22456.

[25] H. Wang, H. Wang, S. Chen, B. Zhang, G. Yang, P. Gao, J. Liu, X. Fan, Y. Huang, J. Lin, et al., *ACS Appl. Energy Mater.* **2019**, *2*, 7942–7951.

[26] Z. Zhang, X. Li, C. Wang, S. Fu, Y. Liu, C. Shao, *Macromol. Mater. Eng.* **2009**, *294*, 673–678.

[27] A. Sadezky, H. Muckenhuber, H. Grothe, R. Niessner, U. Pöschl, *Carbon N. Y.* **2005**, *43*,

1731–1742.

[28] S. Yarova, D. Jones, F. Jaouen, S. Cavaliere, *Surfaces* **2019**, *2*, 159–176.

[29] I. Savych, J. Bernard d'Arbigny, S. Subianto, S. Cavaliere, D. J. Jones, J. Rozière, *J. Power Sources* **2014**, *257*, 147–155.

[30] G. Ercolano, F. Farina, S. Cavaliere, D. J. Jones, J. Rozière, *J. Mater. Chem. A* **2017**, *5*, 3974–3980.

[31] L. Madec, V. Gabaudan, G. Gachot, L. Stievano, L. Monconduit, H. Martinez, *ACS Appl. Mater. Interfaces* **2018**, *10*, 34116–34122.

[32] J. Wang, J. Polleux, J. Lim, B. Dunn, *J. Phys. Chem. C* **2007**, *111*, 14925–14931.

[33] T. W. Zerda, W. Xu, H. Yang, M. Gerspacher, *Rubber Chem. Technol.* **1998**, *71*, 26–37.

[34] A. C. Ferrari, D. M. Basko, *Nat. Nanotechnol.* **2013**, *8*, 235–246.

[35] C. Hu, S. Sedghi, A. Silvestre-Albero, G. G. Andersson, A. Sharma, P. Pendleton, F. Rodríguez-Reinoso, K. Kaneko, M. J. Biggs, *Carbon N. Y.* **2015**, *85*, 147–158.

[36] K. Bogdanov, A. Fedorov, V. Osipov, T. Enoki, K. Takai, T. Hayashi, V. Ermakov, S. Moshkalev, A. Baranov, *Carbon N. Y.* **2014**, *73*, 78–86.

[37] A. C. Ferrari, J. Robertson, *Phys. Rev. B* **2000**, *61*, 14095–14107.

[38] A. Zani, D. Dellasega, V. Russo, M. Passoni, *Carbon N. Y.* **2013**, *56*, 358–365.

[39] Z. Li, C. Bommier, Z. Sen Chong, Z. Jian, T. W. Surta, X. Wang, Z. Xing, J. C. Neuefeind, W. F. Stickle, M. Dolgos, et al., *Adv. Energy Mater.* **2017**, *7*, 1602894.

[40] S. Alvin, D. Yoon, C. Chandra, H. S. Cahyadi, J.-H. Park, W. Chang, K. Y. Chung, J. Kim, *Carbon N. Y.* **2019**, DOI 10.1016/J.CARBON.2018.12.112.

[41] D. Datta, J. Li, V. B. Shenoy, *ACS Appl. Mater. Interfaces* **2014**, *6*, 1788–1795.

[42] P. Tsai, S.-C. Chung, S. Lin, A. Yamada, *J. Mater. Chem. A* **2015**, *3*, 9763–9768.

[43] J. C. Chacón-Torres, L. Wirtz, T. Pichler, *ACS Nano* **2013**, *7*, 9249–9259.

[44] M. A. Pimenta, G. Dresselhaus, M. S. Dresselhaus, L. G. Cançado, A. Jorio, R. Saito, *Phys. Chem. Chem. Phys.* **2007**, *9*, 1276–1290.

[45] D. Yoon, J. Hwang, W. Chang, J. Kim, *ACS Appl. Mater. Interfaces* **2018**, *10*, 569–581.

[46] S. Qiu, L. Xiao, M. L. Sushko, K. S. Han, Y. Shao, M. Yan, X. Liang, L. Mai, J. Feng, Y. Cao, et al., *Adv. Energy Mater.* **2017**, *7*, 1700403.

[47] E. M. Lotfabad, J. Ding, K. Cui, A. Kohandehghan, W. P. Kalisvaart, M. Hazelton, D. Mitlin, *ACS Nano* **2014**, *8*, 7115–7129.

[48] P. Mallet-Ladeira, P. Puech, C. Toulouse, M. Cazayous, N. Ratel-Ramond, P. Weisbecker, G. L. Vignoles, M. Monthioux, *Carbon N. Y.* **2014**, *80*, 629–639.

[49] T. Zerda, W. Xu, *Rubber Chem. …* **1998**, *71*, 26–37.